Experimental study of granular convection

James B. Knight, E. E. Ehrichs,* Vadim Yu. Kuperman, Janna K. Flint, Heinrich M. Jaeger, and Sidney R. Nagel
The James Franck Institute and Department of Physics, The University of Chicago, Chicago, Illinois 60637
(Received 4 October 1995)

Dry granular material confined to a cylindrical vessel convects when subjected to either continuous or discrete vertical oscillations of sufficient intensity. Particles flow upward in the center of the container and fall in a thin stream along the wall. We have studied this motion experimentally in three-dimensional cylinders for a variety of material, container, and vibration parameters using tracer particle techniques and magnetic resonance imaging. By combining these methods, we have characterized both the depth and radial dependence of the vertical flow velocity. We find that the upward flow velocity along the cylinder axis decays exponentially from the top free surface into the bulk of the material. This flow decreases and changes direction as the inner container walls are approached, displaying a radial dependence closely approximated by either a hyperbolic cosine or a modified Bessel function of order zero. We propose a simple model of granular convection consistent with these findings. [S1063-651X(96)10110-0]

PACS number(s): 46.10.+z, 47.27.Te, 64.75.+g, 87.59.Pw

I. INTRODUCTION

Dry, cohesionless granular materials are composed of a large number of solid particles typically of sufficient size that thermal energy is negligible as compared to gravitational energy [1]. Gravity consolidates the particles into a static pile, while mechanical agitation induces motion. One dynamic instability, granular convection, arises from vertical oscillations. Below a threshold vibration acceleration, no flow is observed and the material behaves as a solid; above this threshold, the particles convect in a pattern determined by the container geometry. In a cylinder, they rise in the center and fall in a thin stream down the container walls [2].

Convection in vibrated granular materials has attracted scientific attention since Faraday first reported the phenomenon in 1831 [3]. This is due in part to the importance of the flow behavior of particulate solids to many industrial and geophysical processes [4]. For example, convection is a mechanism for size segregation in granular mixtures, a phenomenon that plagues a variety of industrial mixing procedures [2]. Granular convection embodies the essential ambiguity in the behavior of granular materials, as the onset of a convective state implies a transition from solid- to liquidlike behavior. A comprehensive description of the granular state must capture this feature. Despite the avalanche of theoretical [5,6] and computational [7–9] work on granular dynamics in the physics community, no equation of motion, analagous to the Navier-Stokes equation for fluids, has been firmly established for all regimes of granular flow. Granular convection, with its similarities to fluid motion, offers an analogy from which to begin.

Here we address this issue with a systematic experimental investigation of granular convection. Our results allow a quantitative analysis of the flow profiles established by the convective instability. The convection velocity decays exponentially in depth, with a length and a time scale dependent on the shaking parameters. The radial variation of the velocity is fit equally well with either a hyperbolic cosine or a modified Bessel function of order zero. These results can serve as benchmarks for the development of a comprehensive theoretical framework for granular convection.

Experimental observations of granular flow are complicated by the opacity of the material. As a consequence, most work on granular convection in three dimensions has focused on external features of the flow, such as heaping [10–14]. Alternatively, individual particles can be easily tracked in two-dimensional systems [15,16]. The applicability of results from these studies to actual three-dimensional flow is, however, limited because of additional frictional interactions with the front and back container walls and by phenomena unique to two dimensions such as the crystallization of round particles into a hexagonal close-packed array [17]. Fully three-dimensional flow has typically been studied invasively with tracer particles or with low-resolution imaging techniques [18]. Recently, however, magnetic resonance imaging (MRI) has been successfully applied as a high-resolution, noninvasive probe of granular flow [19,20].

In this paper, we employ tracer particles and magnetic resonance imaging (MRI) to characterize granular convection in a vibrated cylinder and track the flow over a wide range of physical parameters. Section II contains a description of the tracer particle technique, which was used to measure the depth dependence of the flow near the container axis, and the data obtained therewith. We introduce a characteristic time and length scale for the flow and show scaling of the data. Section III describes the MRI method and the observations of the radial dependence of the flow obtained through its use. A detailed discussion of all of these results is presented in Sec. IV, where we also describe simple, empirical models which reproduce the experimental results. Section V contains the conclusion.

II. TRACER PARTICLE EXPERIMENTS AND RESULTS

Experimental Setup. The tracer particle experiments used a vertical Lucite cylinder of inner radius $R=28.5$ mm that was carefully leveled on a vibration test systems VG100 vibration exciter [21]. A layer of glass beads with diameter

*Present address: Advanced MicroDevices, 5204 East Ben White Boulevard, Austin, TX 78741.

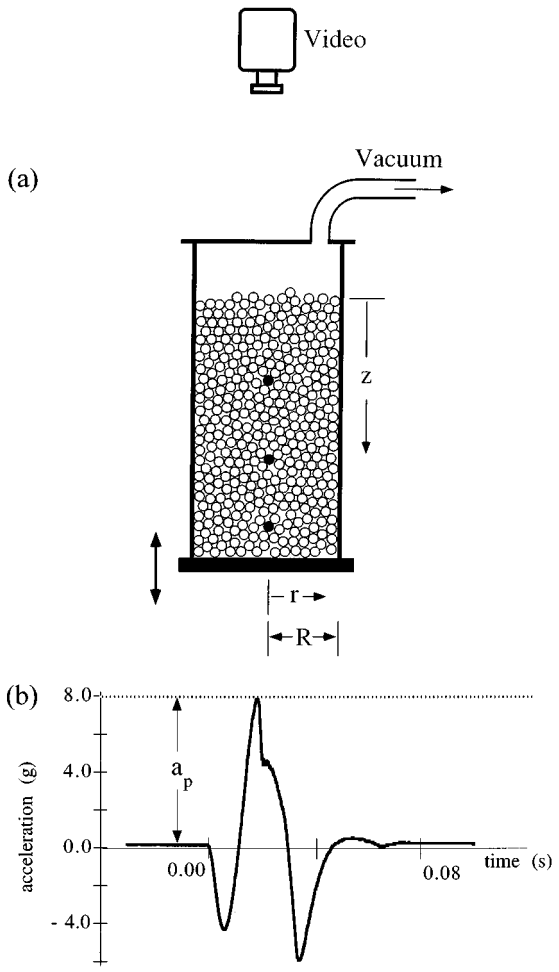

FIG. 1. (a) A schematic drawing of the apparatus showing a slice through the center of the cylindrical container and the corresponding cylindrical coordinate system. (b) The acceleration induced by a tap of $\Gamma=8$ for the tracer bead experiments. This profile was obtained with an accelerometer mounted on the stage of the vibration exciter, and is the average of 64 taps.

$d=0.5$ mm was epoxied to the interior walls to control friction and thus insure reproducible flow. The cylinder was filled to a total height of about 200 mm with clean, monodisperse glass beads; as these particles were added, dyed glass beads were placed along the central axis of the cylinder at several depths as shown schematically in Fig. 1(a). We use a cylindrical coordinate system in which the depth from the surface is measured by z and the radial position by r.

After preparation, the cylinder was subjected to controlled, vertical shakes (''taps'') separated by a waiting period sufficiently long for particle movement to cease. In other experiments, the cylinder was shaken continuously. Each tap was generated by feeding one cycle of a sine wave of frequency f into the vibration exciter; for continuous shaking, the full sine wave was used. A PCB Piezotronics model 303A03 accelerometer fixed to the container base and connected to a storage oscilloscope monitored the tapping acceleration. A representative trace of a single tap is shown in Fig. 1(b). The distortion from the original sinusoidal input is due to the dynamic response of the shaker under an applied load. We parameterize the strength of the applied acceleration by Γ, the dimensionless ratio of the peak acceleration a_p to that of gravity, $g=9.8$ m/s^2: $\Gamma=a_p/g$ [22]. A time lapse video camera recorder (VCR) was employed to observe the top surface of the container over long periods of time (up to two weeks) and record the rise time t of each tracer bead. We define t as the time, in units of number of taps, it took a tracer bead to move to the surface.

Humidity fluctuations induced significant changes in the flow speeds for nonevacuated systems. Therefore, upon completion of the loading process, the cylinder was evacuated (to about 10 Torr). Sufficient space remained above the top layer of particles so that they did not strike the container lid during vibration.

Results. Figure 2(a) shows representative data collected in this manner for $d=3.5$ mm beads. The starting depths z/d, normalized to the bead diameter, of several tracers are plotted against t for different values of the acceleration. The frequency of the taps, which were applied discretely, was held constant at $f=30.5$ Hz. It is important to note that f describes the frequency of each individual tap, and not the rate at which the the taps were applied. The repeat rate of the taps was chosen to permit complete mechanical relaxation between shakes; typically, taps were separated by at least 0.5 s. The axes in Fig. 2 are oriented such that the origin, corresponding to a bead on the top surface, is at the upper right of the graph. A logarithmic time axis is necessary to view all the data, as the rise time increases dramatically with decreasing Γ. Each curve is composed of at least two-separate experiments (for some values of Γ four separate runs were made); the consistency of the data confirms the reproducibility of properly controlled granular convection.

We have verified that interactions between the particles and the interstitial air do not influence the motion by using tracer beads to observe convection at atmospheric pressure, 10 Torr, and 0.5 Torr while otherwise maintaining identical physical conditions ($d=1.5$ mm, $\Gamma=3.5$, $f=30.5$ Hz). The flow at each pressure was indistinguishable, with the exception that the lower pressure runs were slightly faster. We attribute this to the evaporation of moisture from the surface of the particles under vacuum [23].

While Γ is the control parameter for granular convection most often cited in the literature, f also influences flow. Figure 2(b) shows data collected and displayed in the same manner as that shown in Fig. 2(a), but with acceleration held constant and frequency varied. The flow speed depends sensitively upon frequency, decreasing rapidly as f is increased.

At long times, each curve in Figs. 2(a) and 2(b) approaches a logarithmic form. The solid lines through each data set are fits to

$$z(t,r=0)=\xi \ln\left(1+\frac{t}{\tau}\right), \tag{1}$$

where ξ and τ are a length and a time scale describing the convective flow. The tracer particle technique limits measurements to the central axis of the cylindrical container, which is why we have specified $r=0$ in Eq. (1).

The depth dependence of the upward velocity is found by taking the time derivative of data such as in Figs. 2(a) and 2(b). This is the ''average'' velocity of the particles, in the sense that it describes the net motion of a particle from one

tap to the next. The instantaneous velocity during a tap, when the container is in motion, may be quite different. Figure 2(c) shows the exponential decay with depth of the upward velocity explicitly. The local slope of the curves in Fig. 2(a), which is $v(z,r=0)$, is plotted on a logarithmic scale against depth. The solid lines are given by

$$v(z,r=0)=\frac{\xi}{\tau}e^{-(z/\xi)}, \tag{2}$$

which is obtained from Eq. (1) by differentiating $z(t)$ and eliminating t. The lines in Fig. 2(c) use the same values for ξ

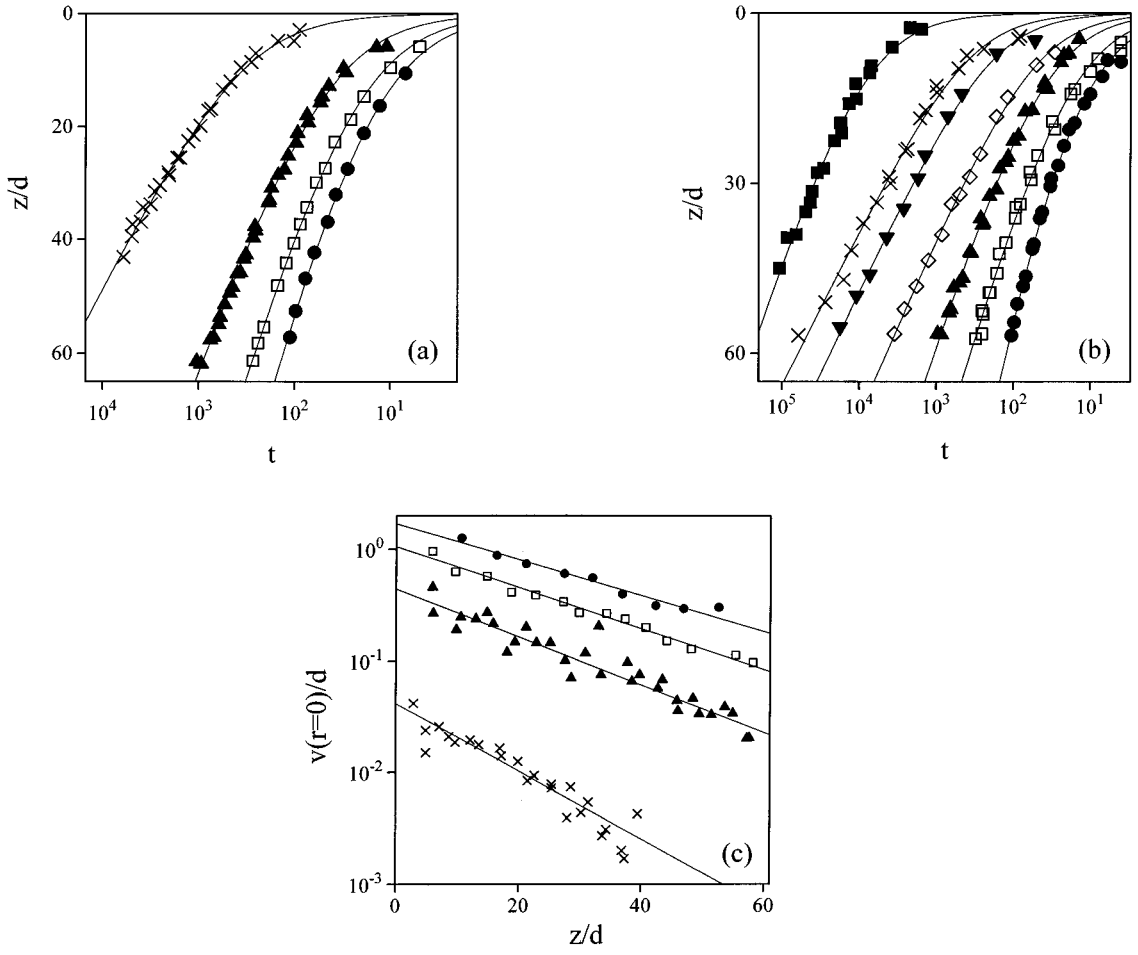

FIG. 2. (a) The initial depth z/d (where z is measured from the top surface and normalized to units of bead diameter d) of several tracer beads plotted against the logarithm of the time t (in units of ''taps'') required for each to rise to the surface. The dyed tracer particles, which were dyed glass balls of diameter $D=4.0$ mm, were carefully placed in the center of the container at several depths as the surrounding particles of diameter $d=3.5$ mm were poured in. The axes are oriented such that the origin is in the upper right of the plot. The frequency of the taps, which were applied discretely, was held constant at $f=30.5$ Hz, while the acceleration Γ was varied to $\Gamma=3.0$ (×), $\Gamma=6.0$ (▲), $\Gamma=9.0$ (□), and $\Gamma=12.0$ (●). The data from at least two separate runs are shown for each value of Γ. Up to nine tracer particles, separated in depth by at least 20 mm, were used in a single run. The solid lines through the data are least-square fits to Eq. (1). (b) The initial depth of several tracer beads plotted against the logarithm of the rise time for $\Gamma=6.0$ and $f=15$ Hz (●), $f=20$ Hz (□), $f=26$ Hz (▲), $f=35$ Hz (◇), $f=50$ Hz (▼), $f=60$ Hz (×), and $f=100$ Hz (■). These data were collected in the same manner as that in (a), with the exception that frequency was varied while acceleration was held constant. The solid lines are least-square fits to Eq. (1). (c) The logarithm of the upward flow velocity in the center of the container, $v(z,r=0)/d$ (in units of bead diameters per tap), plotted against the dimensionless depth z/d. The velocity was calculated from the local slope of the data in (a). The solid lines were generated by inserting the parameters ξ and τ from the least-square fits shown in (a) into Eq. (2). We emphasize that $v(z,r=0)$ is not the instantaneous velocity of a particle during a tap; instead, it is a measure of the cumulative motion from tap to tap. (d) The scaled depth z_s ($z_s=z/\xi$) plotted against the logarithm of the scaled time t_s ($t_s=t/\tau$) for data collected under a wide range of physical parameters. The plot is composed of individual curves of the form shown in (a) and (b) collected for $1.5\leqslant\Gamma\leqslant13.0$, 10 Hz$\leqslant f\leqslant$100 Hz, 1.0 mm$\leqslant d\leqslant$3.5 mm, and both discrete and continuous shaking. The dotted-line is a fit to Eq. (1) with $\xi=1$ and $\tau=1$. (e) The initial depth of several tracer particles plotted against the logarithm of the rise time for $\Gamma=3.7$, $d=1.5$ mm, and three different aspect ratios α (α is the ratio of the column height to the container diameter): $\alpha=1$ (×), $\alpha=2$ (□), and $\alpha=3$ (○). The dotted line is a least square fit to Eq. (1) of the $\alpha=3$ data near the top of the column ($z/d<75$). The inset of (e) is a plot of the scaled depth against the logarithm of the scaled rise time for data collected at $f=30.5$ Hz and several values of Γ for $d=1.0$ mm ($\Gamma=12.0$, 10.5, 9.0, 6.0, and 4.5) and $d=2.0$ mm ($\Gamma=12.9$, 10.5, 7.4, 6.0, and 4.5). The dotted line is a fit to Eq. (1) with $\xi=1$ and $\tau=1$. The outliers from this fit are contained within the $\Gamma=6.0$ and $\Gamma=4.5$ data for both particle sizes.

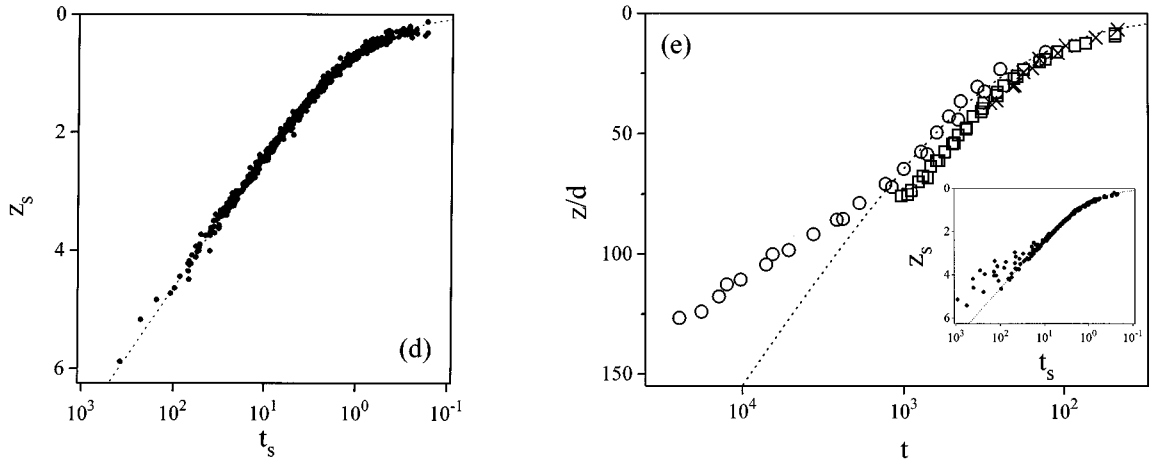

FIG. 2 (*Continued*).

and τ as calculated from the fits to Eq. (1) in Fig. 2(a). The excellent agreement thus provides an additional consistency check.

Scaling. Data such as that shown in Figs. 2(a) and 2(b) were collected over a wide range of accelerations ($1.5 \leqslant \Gamma \leqslant 13.0$), frequencies (10 Hz$\leqslant f \leqslant$100 Hz), and particle sizes ($d=1.0$ mm, 2.0 mm, and 3.5 mm). We measured the convection parameters using both discrete taps as well as a continuous oscillation. In almost all cases, the results were fit well by Eq. (1); the exceptions will be discussed in the next paragraph. To illustrate this, Fig. 2(d) shows a ''master'' curve constructed by scaling many individual curves in a manner reflective of Eq. (1). The depth z is scaled by the length scale ξ, $z_s=z/\xi$, while time is scaled by the time constant τ, $t_s=t/\tau$. The dotted line represents the scaled form of Eq. (1) (638 individual data points are included). For this data, the scaling is successful over at least three decades in scaled time and six length scales in depth, emphasizing that Eq. (1) is a good description of granular convection over a wide range of physical parameters.

We observe systematic deviation from Eq. (1) near the bottom of the container in relatively slow flow. In this limit, we have also noted a dependence on the aspect ratio of the material, where the aspect ratio α is the ratio of the column height H to the container diameter $2R$: $\alpha=H/2R$. Figure 2(e) is a plot of depth z/d versus t for $d=1.5$ mm and $\Gamma=3.7$. Data for three values of α are shown. Each curve consists of data acquired in at least two separate runs. While the $\alpha=1$ and $\alpha=2$ curves exhibit the characteristic logarithmic form, the $\alpha=3$ data deviates from Eq. (1) near the bottom of the container. The dotted line through the $\alpha=3$ data is a best fit to the data near the top of the container ($z/d \leqslant 75$). The $\alpha=3$ curve is also systematically slower than both the $\alpha=1$ and $\alpha=2$ cases.

The inset of Fig. 2(e) shows the effect of this deviation from the scaling implied by Eq. (1). The scaled depth z_s is plotted against the logarithm of the scaled rise time t_s for all the data collected using the $d=1.0$ mm and $d=2.0$ mm particles at constant frequency ($f=30.5$ Hz) and varying Γ. As in Fig. 2(d), the dotted line again represents the scaled form of Eq. (1). The outliers apparent for $z_s>2$ are from data collected at the two lowest accelerations: $\Gamma=4.5$ and 6.0.

Parameter Dependence. Equation (1) yields two parameters with which to describe granular convection, a length ξ and a time scale τ, and each depends on Γ and f, in addition to particle size and other physical parameters. Figure 3(a) shows the acceleration dependence of ξ/d, for three sizes of particles: $d=1.0$ mm, 2.0 mm, and 3.5 mm. To generate this data, the wave form frequency was fixed to 30.5 Hz and Γ was varied. The resulting depth versus time curves were then fit to Eq. (1) to obtain ξ. For the four curves in which a systematic deviation from Eq. (1) was observed near the bottom of the container ($d=2$ mm, 3 mm; $\Gamma=4.5$, 6.0), only the portion consistent with Eq. (1) was fit. Typically, this consisted of restricting the fit to $z/d<75$, and the error bars in Fig. 3(a) reflect the uncertainty in the fits over this parameter range. The inclusion of all of the data for these four curves (i.e., including data for $z/d>75$) would result in considerably lower values of ξ and larger error bars. The normalized length scale ξ/d decreases with increasing particle size and increases linearly with increasing acceleration [the dotted lines in Fig. 3(a) are linear fits to the data]. The unnormalized length scale ξ increases with larger d.

The frequency dependence of ξ was obtained in a similar manner. The frequency f was varied at a fixed acceleration, and ξ was obtained from the resulting depth versus time plots. Figure 3(b) is a plot of ξ versus $1/f^2$ for $d=3.5$ mm beads and several values of Γ. The curves appear linear with this choice of axes, with the slope increasing with Γ. By combining the Γ and f dependence of ξ, we find that ξ depends linearly on A, the amplitude of the taps, $\xi \propto \Gamma/f^2 \propto A$, where we have used the relation $\Gamma \propto A f^2$, which is valid for a continuous sine wave acceleration. This is a reasonable result, as the amplitude of the vibration comprises a natural length scale of the system.

Figure 4(a) is a plot of the time scale τ versus acceleration for 1.0 mm, 2.0 mm, and 3.5 mm beads. These values were obtained from the same fits, described above, used to establish $\xi(\Gamma)$ [Fig. 3(a)]. Although the data range is insufficient to fit a power law with any confidence, the data is consistent with a divergence around $\Gamma \approx 1$. In Fig. 4(a), the time constants have been scaled by dividing through by the particle size d. The resulting collapse of the data onto a single curve suggests that τ is proportional to d.

The frequency dependence of τ is illustrated in Fig. 4(b), where τ is plotted on a log scale versus f for several values

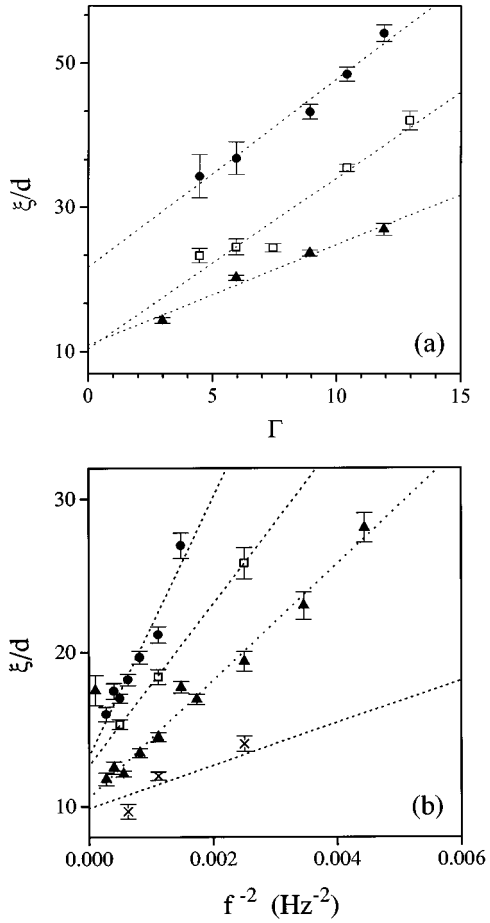

FIG. 3. (a) The length scale ξ/d is plotted against the dimensionless acceleration Γ for three particles sizes: $d=1.0$ mm (●), $d=2.0$ mm (□), and $d=3.5$ mm (▲). The dotted lines are least-square fits to $\xi/d \propto \Gamma$. Least square fits to Eq. (1) of data such as that shown in Fig. 2(a), in which the frequency f was held constant at 30.5 Hz, were used to determine ξ, and the error bars reflect uncertainty in these fits. (b) The length scale ξ/d is plotted against f^2 (in units of Hz^{-2}) for $d=3.5$ mm and $\Gamma=3.0$ (×), 4.5 (▲), 9.0 (□), and 12.0 (●). The dotted lines are least-square fits to $\xi/d \propto f^{-2}$. Least-square fits to Eq. (1) of data such as that shown in Fig. 2(b), in which the acceleration was held constant and the frequency was varied, were used to determine ξ/d. As in (a), the error bars were calculated from the statistical uncertainty in these fits.

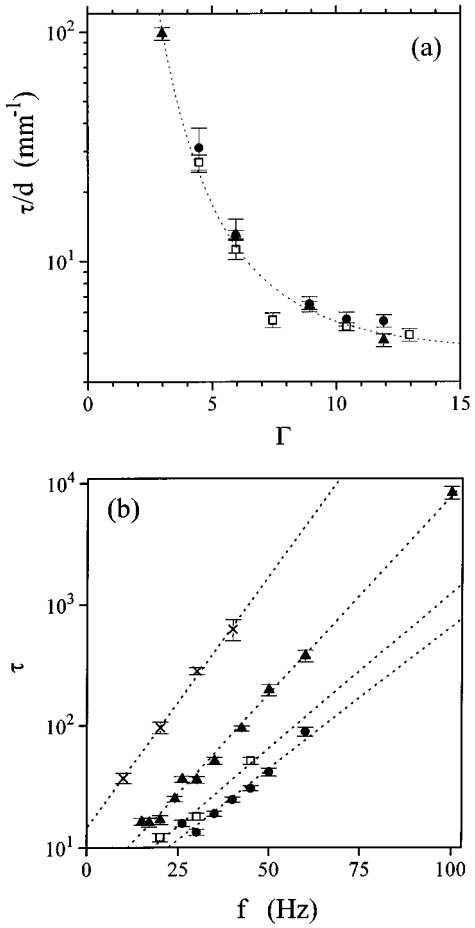

FIG. 4. (a) The logarithm of the time scale τ, scaled by the particle diameter d, is plotted against the acceleration for three particle sizes: $d=1.0$ mm (●), $d=2.0$ mm (□), and $d=3.5$ mm (▲). The dotted line is a least-square fit to $\tau/d \propto (\Gamma-\Gamma_c)^{-\beta}$, with $\Gamma_c \approx 1.2$ and $\beta \approx 2.5$. The time scale was calculated using the same fits described in Fig. 3(a). (b) The logarithm of the time scale is plotted against the frequency for $d=3.5$ mm and $\Gamma=3.0$ (×), 4.5 (▲), 9.0 (□), and 12.0 (●). The dotted lines are fits to the form $\tau \propto \exp(f/f_0)$. The time scale was calculated using the same fits described in Fig. 3(b).

of Γ. The dotted lines are fits to $\tau \propto \exp(f/f_0)$. (A plot of τ against f^{-2} gives poor results and rules out any simple amplitude dependence.) The characteristic frequency f_0 increases slowly and monotonically with acceleration, with a typical value being $f_0 \approx 35$ Hz for $\Gamma=6.0$. This is roughly the frequency obtained by considering the time scale of a bead falling its own diameter d (in this case $d=3.5$ mm) under the influence of gravity: $f_d \approx (g/d)^{0.5} \approx 50$ Hz.

III. MAGNETIC RESONANCE IMAGING EXPERIMENTS

Experimental Setup. While experiments with tracer beads are sufficient to measure the flow characteristics in the center of the cylinder, magnetic resonance imaging provides a high-resolution, noninvasive probe of motion throughout the sample. We used MRI to obtain velocity flow profiles in three Lucite cylinders of inner radius $R=6.4$ mm, 12.7 mm, and 19.1 mm [24]. The cylinders were filled with poppy seeds and placed on a nonmetallic sample platform within the bore of a GE/Bruker 4.7 T MRI magnet. Nakagawa *et al.* have shown that oil-containing seeds provide sufficient free protons in the liquid state to produce a discernible magnetic resonance signal [19]; we chose poppy seeds for their small size and dry exterior. The seeds, which were sifted to insure uniformity, were roughly elliptical in shape with a major axis of about 1 mm and a minor axis of 0.7 to 0.8 mm. A layer of seeds was epoxied along the walls of each cylinder to control the friction and to provide a control layer from which to measure motion.

All components within the magnet bore were nonmetallic. The sample platform was coupled through a long, rigid rod to a vibration exciter placed 3 m from the magnet. Nonmetallic linear motion guides were used to insure vertical shaking. Only discrete taps were attainable with this system. All of the MRI data presented in this paper was taken at $f=20$ Hz; because of the mechanical limitations of the shaking

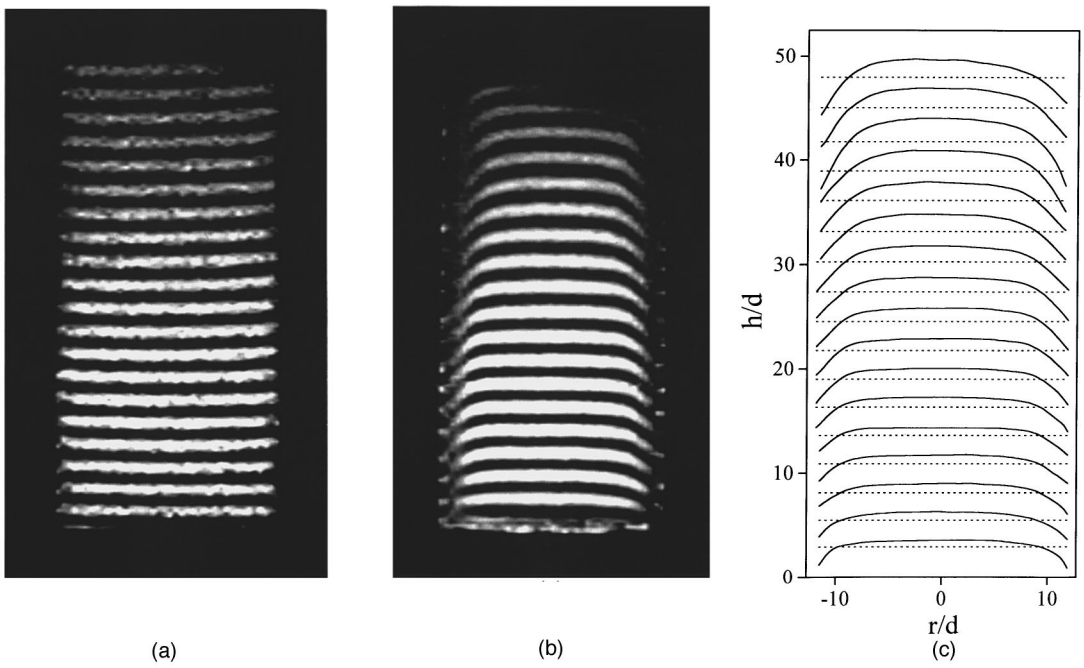

FIG. 5. (a) Magnetic resonance image of a 3 mm slice through the center of an unshaken acrylic cylinder ($R/d=12.7$) filled to a height of 52.5 mm with white poppy seeds ($d\approx1$ mm). Bright areas in the image correspond to the peaks of the sinusoidally varying longitudinal spin polarization. The slight curvature in the horizontal ''stripes'' is a consequence of inhomogeneities in the local magnetic field. (b) Magnetic resonance image showing the deformation of this spin-tagging pattern after one tap with $\Gamma=6$. Because of the rapid decay of the spin-tagging pattern, 256 identical shakes are necessary to obtain a single image, and (b) is an average of 8 such images. (c) The peak positions of the spin-tagging stripes in (b). The dotted lines represent the unperturbed position of the stripes. Both the peak positions and the control lines have been corrected for erroneous curvature due to magnetic field inhomogeneities.

mechanism, frequency could not be varied over as wide a range as in Sec. II. The magnitude of the applied acceleration was measured with an accelerometer. Mechanical resonances complicate the pulse shapes, but they are reproducible and result in convection qualitatively similar to that of sinusoidal oscillations. Individual pulse profiles are of the same general shape as that shown in Fig. 1(b), but with more fine structure. The peak acceleration a_p used to parametrize the intensity of the applied force is defined in the same way as in Fig. 1(b), and the convection parameters obtained in tracer particle and MRI experiments at the same Γ are comparable.

Flow Profiles. We employed a spin-tagging technique to visualize flow profiles within the containers. [25] Seeds were ''tagged'' selectively by modulating the longitudinal spin polarization in the vertical direction. An example of the resulting horizontal stripe pattern is shown in Fig. 5(a), which is an MRI image of a 3 mm thick slice through the center of an unshaken $R=12.7$ container. Bright areas in the image correspond to the peaks of the sinusoidal modulation. The slight curvature of the stripes, a consequence of inhomogeneities in the magnetic field, can easily be corrected in later data analysis. Thermal randomization of the spins limits the persistence of this pattern, which decays exponentially with the spin-lattice relaxation time T_1. For poppy seeds in a 2.0 T field, $T_1\approx200$ ms. [20] Because of the rapid decay of the spin-tagging pattern, separate phase-encoded gradient echoes from multiple pattern applications are necessary to construct a complete image. We collect one vertical column of data in an image after each application of the pattern; thus a horizontal resolution of 256 columns requires 256 separate spin-tagging and read sequences.

Figure 5(b) is an image of the flow arising from a single shake with $\Gamma=6$ and $f=20$ Hz. The stripes have bent in a manner consistent with particle motion upward in the middle of the container and downward along the sides. The layer of seeds glued to the walls has not moved, and these particles, along with the control stripes in Fig. 5(a), serve as references from which to measure the deformation of the bands. Figure 5(b) is an average of eight images, collected one immediately after another, each with a horizontal resolution of 256 columns; thus 2048 separate taps contributed to this image. The taps were applied between the application of the spin-tagging pattern and the read sequence, and were separated by 0.7 s pauses to allow the system to relax both magnetically and mechanically. The clarity of the stripes is striking evidence of the reproducibility of the applied excitations and of the upward seed motion in the central part of the flow. The blurriness in the image near the walls is a consequence of particle diffusion [26], the implications of which will be discussed in Sec. IV.

Figure 5(c) shows the peak positions of the flow lines (solid lines) extracted from the image in Fig. 5(b). The dotted lines represent the unperturbed position of the stripes. Both the flow lines and the control lines have been corrected to remove erroneous curvature resulting from magnetic field inhomogeneities. The vertical axis is dimensionless depth z/d (where $d=1$ mm is the average poppy seed diameter), and the horizontal axis is the dimensionless radial position r/d. The lateral boundaries of the plot frame correspond to the internal edge of the container. The epoxied layer of seeds lies within this boundary, and so the flow lines are resolved to within almost one seed diameter of the walls.

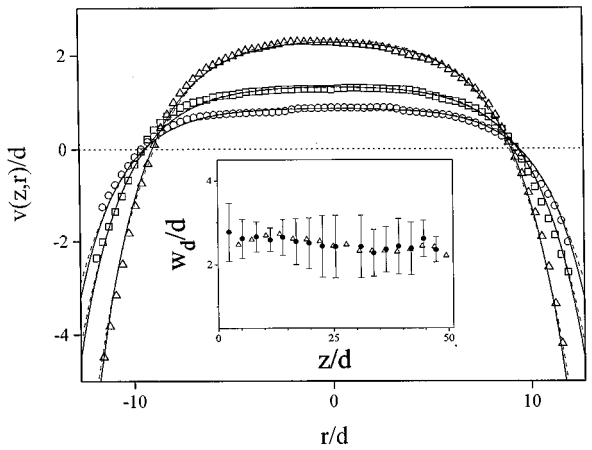

FIG. 6. The velocity $v(z,r)/d$ (in units of bead diameters per tap) in a container with $R/d=12.7$ and $\Gamma=6$ is plotted against the radial coordinate r/d for three depths: $z/d=9.2$ (△), $z/d=26.5$ (□), and $z/d=42.8$ (○). The velocity was calculated by subtracting the control lines in Fig. 5(c) from the peak positions. The dotted line identifies $v(z,r)/d=0$. The solid lines through the data are least square fits to Eq. (3a); the dashed lines are fits to Eq. (3b). The inset shows the width of the downward flow, w_d/d, plotted against depth for $\Gamma=4$(●) and $\Gamma=8$ (△) in the $R/d=12.7$ container. These values were calculated from the fit parameters v_c, B, and r_c, and the error bars, shown only for the $\Gamma=4$ case, reflect the uncertainty in these fits.

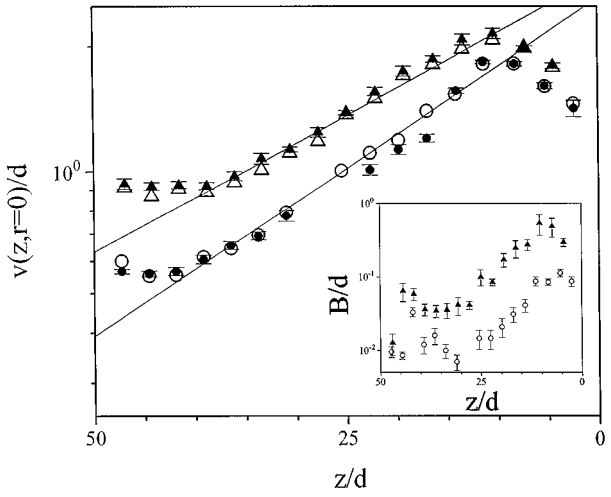

FIG. 7. The logarithm of the upward velocity in the center of the convective flow, $v(z,r=0)/d$, is plotted against depth for $R/d=12.7$ and two values of the acceleration: $\Gamma=4$ (○) and $\Gamma=8$ (△). This data was obtained directly from the magnetic resonance images by subtracting the control lines from the peak positions of the flow lines at $r=0$. The parameter v_c obtained from fits of Eq. (3a) to the individual flow lines are also shown for $\Gamma=4$ (●) and $\Gamma=8$ (▲). The solid lines through the data are least square fits of $v(z,r=0)/d$ to Eq. (2). The inset is a plot of the fitting parameter B as a function of depth for $\Gamma=4$ (○) and $\Gamma=8$ (▲) in the $R/d=12.7$ container.

The velocity, defined as the displacement after a single tap, is calculated by subtracting the control lines from the flow lines. The velocity profiles at three depths ($z/d=9.2$, 26.5, and 42.8) for $R/d=12.7$ and $\Gamma=6$ are shown in Fig. 6. Several key features can be extracted from plots such as this: the magnitude of the upward velocity in the center of the container, which can then be compared with tracer bead data; the width of the downward flowing region w_d, which is not measurable with tracer beads and is essential to the size segregation process; and the radial dependence of the velocity, which is of particular importance in establishing an equation of motion for granular flow. Inspection of Fig. 6 reveals that v decreases rapidly with depth. The individual contours are relatively flat near the center of the container but decrease rapidly near the walls. All three contours cross $v(r,z)=0$ at approximately the same distance from center, thus suggesting that w_d is independent of depth. In the remainder of this section, we will quantify these features.

The solid and dashed lines in Fig. 6 are fits, respectively, to the forms

$$\nu(r)=\nu_c+B\left[1-\cosh\left(\frac{r}{r_c}\right)\right] \tag{3a}$$

and

$$\nu(r)=\nu_c+B\left[1-I_0\left(\frac{r}{r_c}\right)\right], \tag{3b}$$

where v_c, B, and r_c adjustable parameters, and I_0 is a modified Bessel function of order zero satisfying the equation

$$\frac{d^2\nu(\rho)}{d\rho^2}+\frac{1}{\rho}\frac{d\nu(\rho)}{d\rho}-\nu(\rho)=0, \tag{4}$$

with $\rho=r/r_c$. Equations (3) and (4) will be discussed further in Sec. IV.

In previous experiments [20], we used MRI to characterize the depth dependence of the upward velocity of the convective flow in the center of the container $v(z,r=0)$. It was found to decay exponentially with depth into the pile, supporting the tracer bead data [Fig. 2(c)] and Eq. (2). As an example, Fig. 7 is a plot of $v(z,r=0)$ versus z/d for $\Gamma=4$ and $\Gamma=8$ in the $R/d=12.7$ container. The solid lines are fits to Eq. (2) and illustrate exponential decay. We note that these data show the average net displacement after one tap at various positions along the central axis of the container, whereas the data in Sec. II was obtained from the rise times of a tracer particle to the top surface. The fact that both data sets exhibit the same exponential decay serves as an important validity check for the tracer particle method and the applicability of Eq. (2). The agreement between the two sets of data indicate that effects such as compaction or decompaction of the material after the initial preparation, which could influence the tracer particle experiments, were unimportant.

The MRI experiments were limited to comparatively small container sizes and filling heights due to the restrictive physical constraints imposed by the magnet bore. Near the top and bottom of the container in Fig. 7, departures from exponential decay are visible. These are consistent with the roll structure of the convection: particles close to the surface move toward the walls, and their vertical velocity diminishes in favor of horizontal motion; at the bottom, par-

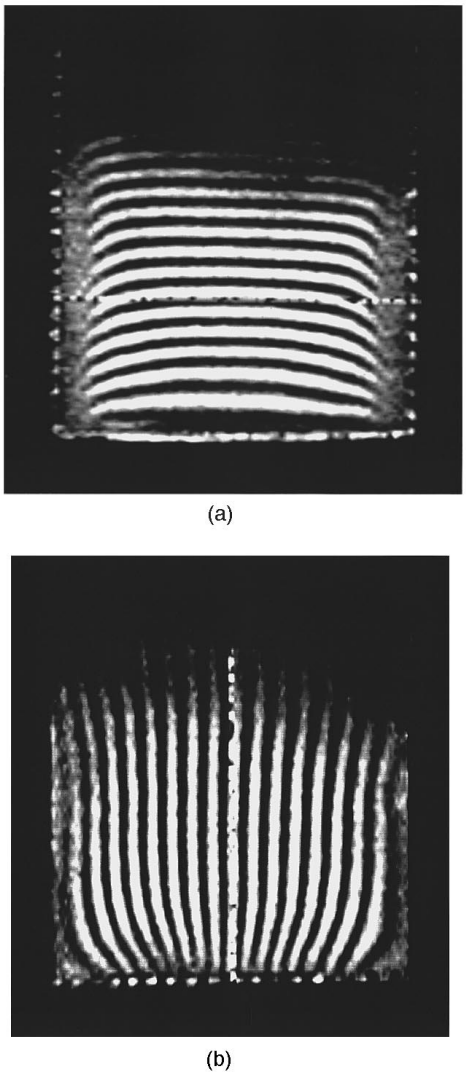

FIG. 8. (a) A magnetic resonance image of a 3 mm slice through the center of the $R/d=19.05$ container showing the deformation of a horizontal spin-tagging pattern after a single shake with $\Gamma=8$. (b) A magnetic resonance image taken under the same conditions as in (a), but showing the deformation of a vertical spin-tagging pattern.

ticles in the downward flow reenter the upward flow collectively due to collisions with the bottom of the container, as opposed to scattering independently from the vertical walls, and this large influx of particles inflates the upward velocity. These effects are exaggerated for fast flow in wide cylinders, where the length scale of the flow is large compared to the height of the column. This situation is shown explicitly in Fig. 8 where we clearly see the deformation of (a) horizontal and (b) vertical spin-tagging patterns after one tap in the $R/d=19.05$ container shaken at $\Gamma=8$. Curvature in the horizontal stripes increases near the bottom of the container, indicating anomolously large upward velocity. The vertical stripes are bent outward near the top (indicating horizontal flow) and bent in at the bottom (indicating flow towards the center).

Width of the downward flow region. Although the magnitude of the velocities varies greatly with depth, the zero intercept, r_o and thus the width $w_d=R-r_o$, of the downward flow does not. This is illustrated in Fig. 6 for the $R/d=12.7$

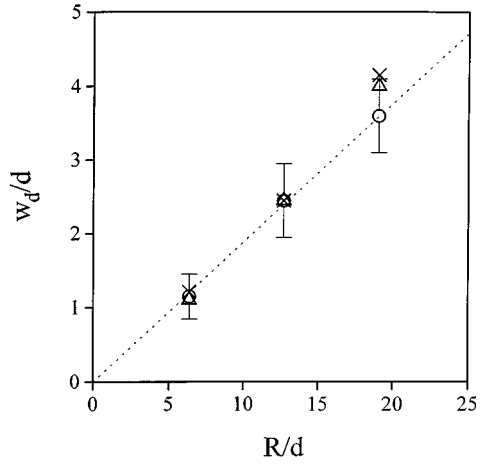

FIG. 9. The width of the downward flowing region, w_d/d, plotted against container radius R/d for $\Gamma=4$ (○), $\Gamma=6$ (×), and $\Gamma=8$ (△). Each value is an average in depth computed from a single image, and the error bars (shown only for the $\Gamma=4$ data) reflect the standard deviation of this average.

container: the velocity profiles of three widely spaced depths intercept the dotted line (corresponding to $v=0$) at the same radius r_o. The inset of Fig. 6 shows this more explicitly. The values of w_d obtained from fits of Eq. (3a) to data such as that shown in the main panel of Fig. 6 are plotted versus depth for two values of Γ. Within experimental error (both systematic and statistical), we find w_d to be independent of both acceleration and depth.

We find, however, that the width of the downward flow region is proportional to container size. Figure 9 illustrates this result with a plot of w_d/d against container radius R/d for several values of Γ. The values of w_d are averages over depth for each container size. The dotted line is a linear fit to the $\Gamma=4$ data, and intercepts $w_d/d=0$ at $R/d=0$ with a slope close to 0.2. The error bars, shown only for the $\Gamma=4$ data, are indicative of the statistical error in the average and the slight systematic difference in w_d on opposite sides of the container in some runs. Asymmetries in the flow can arise if the container is insufficiently level or if the shaking has a horizontal component. (Although the linear motion guides controlled the direction of the taps, levelling the container inside the magnet bore posed some practical difficulty.)

Figure 10 compares the flow in all three containers at $\Gamma=6$. As in Fig. 5(b), these images (pictured to scale with one another) depict the deformation of a horizontal spin-tagging pattern after one tap. All of the velocity contours are fit well by Eqs. (3a) and (3b), and it is the exponentially decaying contribution of the $I_0(r/r_c)$ or $\cosh(r/r_c)$ term that results in the apparently flat regions near the center of the containers.

Figure 11(a) compares the velocity contours at the same depth ($z/d=18$) for all three containers shaken with $\Gamma=8$. The curves are offset to clarify the plot, and the dotted lines intersecting each trace mark $v=0$ and span the container size. The solid line through each curve is a least-squares fit to Eq. (3a). Figure 11(b) shows the same data as in Fig. 11(a) but with different fitting functions.

IV. DISCUSSION

Granular convection in vertically shaken cylindrical containers is characterized by a roll structure. Particles flow up

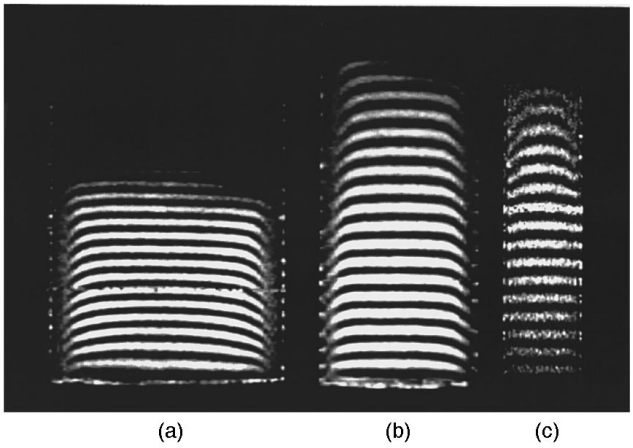

FIG. 10. Magnetic resonance images of a 3 mm slice through the center of the (a) $R/d=19.05$, (b) $R/d=12.7$, and (c) $R/d=6.35$ containers showing the deformation of a horizontal spin-tagging pattern after one shake of strength $\Gamma=6$.

in the center of the container and down along the roughened walls. The velocity of the upward flow decays exponentially from the top surface, and the radial dependence of the flow is strongest near the container walls.

Two fundamental questions regarding granular convection must be addressed: how does flow arise and, once formed, what are the relevant parameters describing its dynamics? Because of the opacity of three-dimensional granular systems, most experimental work has concentrated on the onset of convection, where heaping or some other readily observable phenomenon can be associated with flow. We approach the problem from the opposite perspective: our primary efforts have been to characterize fully developed granular convection, relatively far from onset, by carefully measuring the flow characteristics. In this section, we will discuss our results and compare them to models that, we hope, will provide physical insight into the origins of convection. We will also examine the onset of convection by studying the characteristic length and time scales of the flow.

The role played in convection by the interaction between the particles and the interstitial gas is a subject of considerable debate in the literature. Much of this controversy has arisen from the study of heaping in systems with no effective lateral boundaries [12]. Pak, Van Doorn, and Behringer have resolved much of the controversy by showing that in a vertically shaken torroidal container, heaping is suppressed at gas pressures below about 1 Torr [13]. Small particles ($d\leqslant 0.1$ mm) and a low shaking acceleration ($\Gamma=1.3$) were used. Larger particles ($d\geqslant 1.3$ mm) did not exhibit heaping. In contrast, we find for the container geometries and particles sizes that we have studied that convection is dominated by interactions between the particles and the container walls, and not by interactions between the particles and the interstitial gas. We have verified this explicitly by conducting tracer particle experiments at pressures above and below the threshold reported by Pak, Van Doorn, and Behringer (see Sec. II) [13]. Furthermore, we have also observed changes in the convection pattern induced solely by changes in the boundaries. For example, an asymmetry in the wall friction produces an asymmetric roll, with the particles flowing fastest down the region with highest friction [2]. Changing the

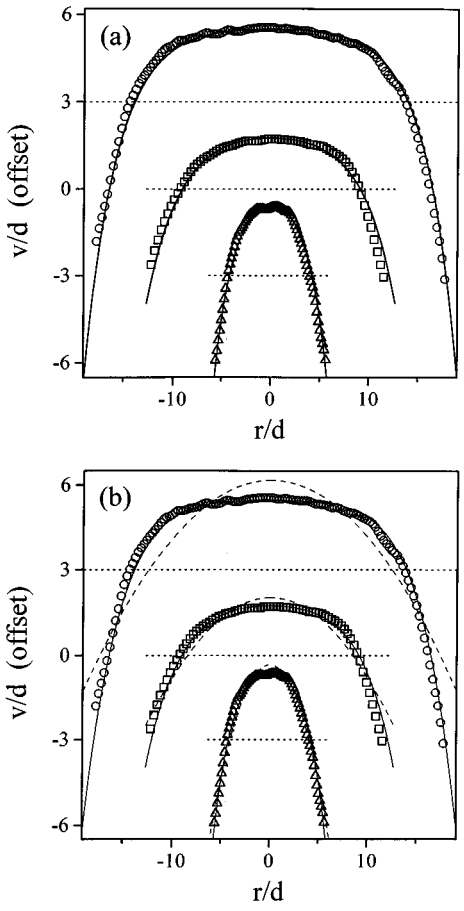

FIG. 11. (a) The velocity (offset for clarity) at $\Gamma=6$ and $z/d=18$ is plotted against the dimensionless radial coordinate r/d for all three containers: $R/d=6.35$ (△), $R/d=12.7$ (□), and $R/d=19.05$ (○). The solid lines are least-square fits to Eq. (3a), and the dotted lines identify $v(z,r)/d=0$ for each curve. (b) The same data as in (a) is shown, but with least-square fits to Eq. (3b) (solid lines) and to a parabolic fitting form (dashed lines).

angle of the walls, so that the container becomes conical or spherical, reverses the sense of the rolls: particles flow up the walls and down in the middle region [2,10,17,27]. We have also found that roll reversal can occur in continuously shaken containers with vertical walls if the wall friction is low. Our identification of the importance of the boundaries is consistent with previous studies of granular convection (both experiments and simulations) in which relatively large particles and containers with significant friction at the lateral boundaries were used [2,7,9,10,15–17,20].

Depth dependence of the axial velocity. Tracer particles [see Fig. 2(c)] and MRI (see Fig. 7) both establish the exponential decay of the upward velocity with depth [Eq. (2)]. A simple model in which convective flow is dominated by scattering from the walls can account for this observation. Flow in the cylinder may be described as having three components: an upward particle flux $j_u(z)$ in the central region; a flux $j_d(z)$ down along the walls; and an inward, transverse flux $j_i(z)$ from the downward flow into the upward flow. The transverse flow could arise from the scattering of particles in the downward flow, either by collisions with other particles or with the wall. The rate of change with depth of the downward flux is proportional to the transverse flux

$$\frac{dj_d(z)}{dz} \propto -j_i(z). \tag{5}$$

If we make the assumption that $j_i(z)$ is directly proportional to the number of particles available to be scattered $j_d(z)$ then

$$\frac{dj_d(z)}{dz} = -pj_d(z), \tag{6}$$

where p is the probability of inward scattering. The simplest assumption regarding p is that it is independent of depth (depending, for example, only on the wall roughness). In this case,

$$j_u(z) \propto j_d(z) \propto e^{-pz}. \tag{7}$$

The two fluxes $j_u(z)$ and $j_d(z)$ are proportional because in steady state the total particle number at any depth is conserved in this system. Since the particle flux is proportional to the velocity, Eq. (7) is equivalent to the empirically derived Eq. (2), where we identify the scattering probability p with the inverse decay length ξ^{-1}.

We directly confirmed the scattering of particles from the downward flow into the upward flow by implanting dyed tracer particles, otherwise indistinguishable from those in the bulk, into the downward flow. Since these tracers moved within a few particles from the translucent container walls, they could be tracked visually. These particles, followed for the duration of their stay in the downward flow, were found to reenter the upward flow over a range of depths, with the average depth of reentry increasing with increasing Γ. The movement of individual particles in the downward flow was noisy, although the average depth dependence was similar to that of the upward flow. These observations support the assumptions of particle scattering and transverse flow made in the model.

Significant deviations from Eq. (1), and thus Eq. (2), are observed for low filling heights at high accelerations (see Fig. 7), and also in relatively tall systems at low Γ for large z/d [see Fig. 2(e)]. The first situation reflects the existence of large convection rolls in the limit that $\xi(\Gamma)$ becomes comparable with the filling height. The mechanism responsible for the deviations is easily detected by MRI and already was discussed in connection with Fig. 7 in Sec. III. The mechanism underlying the second type of deviation is not well established; in part this is due to the exceedingly long runs (order of days to weeks) required to detect bead motion in this limit. Motion near the bottom is slower than Eq. (1) would predict based on a fit to the flow near the top. We have verified that this is not the effect of a size segregation mechanism by varying the diameter of our tracer beads. Indeed, if a size dependent segregation mechanism did affect the data, we would expect that the flow should be faster rather than slower. Within the context of our model, introducing a linear depth dependence to the scattering probability p, $p=p_0+\varepsilon z$, results in the type of deviation we observe experimentally. The assumption of a depth-dependent scattering probability is physically plausible, since near the bottom of a cylinder of particles undergoing very slow convection, one can imagine the collective behavior of the particles to be increasingly solidlike.

Scaling. Figure 2(d) provides clear evidence that the scaling of the data using one time and one length parameter is successful. The need for a two parameter scaling becomes apparent once data over wide ranges of depth, acceleration and frequency are included. Significantly above the onset of convection, the time scale varies little [Fig. 4(a)] with acceleration, while the length scale increases linearly with Γ [Fig. 3(a)]. As a result, the two parameter scaling of the depth vs. time data, using both $\xi(\Gamma)$ and $\tau(\Gamma)$, is well approximated by scaling with only $\xi(\Gamma)$. This is the scaling relation we found in previous work where we had data only in a narrower range of accelerations [2].

The linear dependence of the length scale on the amplitude of the vibration is demonstrated in Fig. 3. The fits in Fig. 3(a) showing the dependence of ξ on Γ for three particle sizes intercept $\xi=0$ at different values of Γ. The data density is not sufficient to define these fits very precisely; indeed, one could make the case that the three lines are roughly parallel, within the scatter. What is clear, though, is that the length scale does not rapidly diminish to zero as the acceleration approaches the critical value of $\Gamma_c \approx 1$. In contrast, the time scale τ appears to diverge as Γ is lowered. The data in Fig. 4(a), which plots τ/d versus Γ, are in fact consistent with a fit of the form $(\Gamma-\Gamma_c)^{-\beta}$. One consequence of the rapidly increasing time scale as Γ is reduced is that experiments which rely upon a finite time frame within which to detect flow or heaping, either to establish the size of the convective instability or its threshold, must eventually fail as Γ approaches Γ_c.

Radial velocity dependence. The most powerful use of MRI is the detailed measurement of the radial dependence of the convection velocity. Figures 6 and 11 show representative velocity profiles. The fits to Eq. (3) were motivated by the strong radial dependence of the velocity near the walls and the axial symmetry of the flow. Both the cosh [shown in Fig. 11(a)] and the I_0 [Fig. 11(b)] fitting forms show excellent agreement with velocity contours from all three cylinders. Other functional forms were also tried but without success. Most power law fits to this data succeed only with large, widely varying powers of r. In particular, parabolic flow profiles [also shown in Fig. 11(b)], which might be expected from comparison with liquid flow through pipes, fit the data reasonably well in the small container but fail for the blunter flow in the larger containers.

Both the hyperbolic cosine and the modified Bessel function fits succeed because they capture the rapid, exponential variation of the velocity near the container walls while providing a nearly flat profile across the center of the flow. The difference between the resulting values for the curvature parameter r_c from either functional form is small and close to the statistical error of the fits. Below, we will motivate the modified Bessel function form by discussing a simple model. We will first discuss the hyperbolic cosine fits, as they give similar results and provide the added advantage that we can easily compare with analytic predictions based on particle conservation.

The fits to the hyperbolic cosine dependence of the radial velocity [Eq. (3a)] have three parameters. v_c, B, and r_c which depend on depth. The agreement between Eq. (3) and the data is excellent, marred only by the asymmetry in some of the velocity contours which is a consequence of the limi-

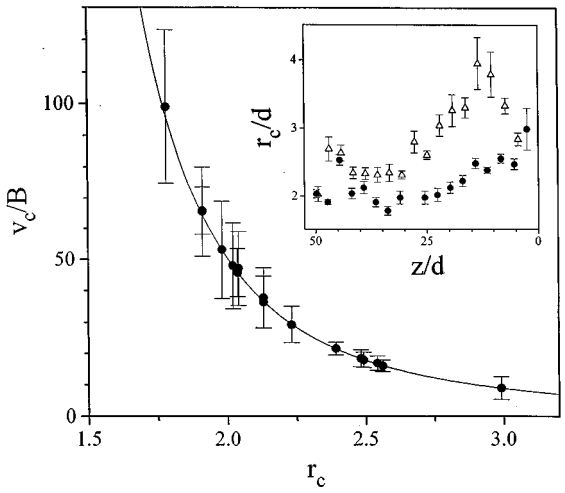

FIG. 12. The dimensionless ratio v_c/B is plotted against r_c/d for $R/d=12.7$ and $\Gamma=4$; the solid line is a fit to Eq. (8). The inset is a plot of the parameter r_c/d against depth for $R/d=12.7$ and $\Gamma=4$ (●) and $\Gamma=8$ (△). The parameters v_c, B, and r_c, described in the text, were calculated from least-square fits to Eq. (3a).

tations on the vertical alignment of the experiment. The axial velocity $v_c=v(z,r=0)$ calculated from fits to Eq. (3) is identical to that measured directly from the raw data; both are plotted in Fig. 7 for comparison. The parameter B, which can be thought of as the amplitude of the curvature term, decays rapidly with depth. The inset of Fig. 7 is a plot of the logarithm of B as a function of depth for two values of Γ in the $R/d=12.7$ container. It can be shown that B is proportional to v_c through a function dependent on container radius and r_c. At any depth within the system, particle number must be conserved, so that

$$\int_0^R \nu(z,r) r \, dr = 0. \tag{8}$$

By imposing this constraint on Eq. (3a), we find that $B=v_c/f(R/r_c)$, where

$$f\left(\frac{R}{r_c}\right)=\frac{\nu_c}{B}=2\left(\frac{r_c}{R}\right)^2\left[1-\cosh\left(\frac{R}{r_c}\right)+\frac{R}{r_c}\sinh\left(\frac{R}{r_c}\right)\right]-1. \tag{9}$$

The agreement between the fitting parameters and this constraint is shown in Fig. 12. The ratio $v_c/B=f(R/r_c)$ is plotted against R/r_c, and the line through the data is a fit to Eq. (9).

The inset of Fig. 12 shows the slow, but significant decrease of the radial length scale r_c with increasing depth. This result at first appears counterintuitive, as one would expect that the flow lines would flatten as the flow velocity decreases. However, over the same depth the amplitude of the curvature term, set by B, diminishes exponentially, overwhelming the slow decrease in r_c and effectively suppressing any visible curvature in the central part of the flow.

From Eq. (3a), the width of the downward flow w_d/d varies with r_c in the following manner:

$$wd/d=R/d-(r_c/d)\cosh^{-1}\left[1+f\left(\frac{R}{r_c}\right)\right]. \tag{10}$$

This does not contradict the independence of w_d on depth observed in the experiments since the depth dependence, through r_c, drops out, as an analysis of the second term on the right hand side of Eq. (10) shows. Over the range relevant to our experiments; $0\leqslant R/r_c<7$, this term is to a very good approximation given by $0.8R/r_c$ [28]. This leaves only a linear dependence of w_d on the container size R in close agreement with the data in Fig. 9. The inset of Fig. 6 shows this explicitly, with a plot of w_d/d, calculated using the fit parameters and Eq. (10), as a function of depth for two accelerations.

The radial [Eq. (3)] and depth [Eq. (2)] dependences can be combined to give a single expression for the flow velocity in terms of ξ, τ, and r_c

$$\nu(r,z)=\frac{\xi}{\tau}\left\{1+\frac{1}{f(R/r_c)}\left[1-\cosh\left(\frac{r}{r_c}\right)\right]\right\}e^{-(z/\xi)} \tag{11a}$$

or

$$\nu(r,z)=\frac{\xi}{\tau}\left\{1+\frac{1}{f_I(R/r_c)}\left[1-I_0\left(\frac{r}{r_c}\right)\right]\right\}e^{-(z/\xi)}, \tag{11b}$$

where f is given in Eq. (9). Here the function $f_I(R/r_c)$ is obtained in the same manner as $f(R/r_c)$. The fitting parameters, particularly r_c, obtained using $I_0(r/r_c)$ in place of $\cosh(r/r_c)$ are of very similar magnitude.

In the absence of a unique functional form that describes the data, further theoretical work is necessary to motivate either the hyperbolic cosine, the modified Bessel function, or some other fit. The modified Bessel function, which solves Eq. (4), is particularly interesting as Bessel functions routinely arise in physical situations involving cylindrical symmetry. Under certain conditions, vibrated granular materials can exhibit some characteristics of a Newtonian fluid [29], and indeed the first two terms of Eq. (4) describe the viscous drag on a Newtonian fluid moving through a pipe [the radial components of the Laplacian of $v(\rho)$: $\nabla_r^2 v(\rho)$]. The final term in Eq. (4), proportional to $v(\rho)$, does not arise from simple fluid mechanics. The depth dependence of the velocity is exponential, so $v(\rho)$ can arise from any force proportional to $v(\rho)$ or a derivative in z of $v(\rho)$. To have the appropriate sign in Eq. (4), this force must oppose viscous drag. If it arises from a viscous force, proportional to $\nabla_z^2 v(\rho)$, then the ''viscosity'' must be negative. A somewhat more intuitive explanation is an effective pressure proportional to $v(r)$ or one of its derivatives in z.

The velocity profiles we have observed with MRI in vibrated cylindrical containers are similar in form to those measured by other means in granular chute flow. A region near the lateral boundaries of the container undergoes a significant variation in velocity while flow near the center is comparatively blunt [30,31]. Nedderman and Laohakul identify a length scale describing the lateral extent of the shear region in vertical chute flow that varies linearly with the wall separation [31]; however, recent work by Pouliquen and Gut-

fraind may not support this observation [32]. In granular convection, we find that the width of the downward flow varies linearly with container radius. These similarities between granular flow induced by different means highlight the central importance of shear at the boundaries for determining flow profiles in fluidized granular material [5,33].

The width of the downward flow has substantial practical interest because of its role in convective size segregation. Consider a mixture of large and small particles confined to a cylindrical geometry and vertically shaken. The large particles rise to the top and stay there, independent of shape or density [34]. One mechanism for this size segregation is convection [2,35]. Large particles are embedded in the upward flow, but upon reaching the top are unable to reenter the relatively thin downward flow. The size of the downward flowing region determines the size of the particles that can be segregated. We have observed that this width w_d is independent of acceleration and depth in a given container. It varies linearly with container diameter, increasing in larger vessels. One possible application of this observation is in the design of containers for separating (or transporting unseparated) particle mixtures.

V. CONCLUSIONS

We have described in this paper a series of experiments measuring the flow characteristics of granular convection. The depth dependence of the upward flow velocity in the center of a cylindrical container was established through measurements of the rise time of tracer particles embedded in the material. The velocity decays exponentially with depth and is described over a wide range of physical parameters by Eq. (2). This behavior is explained by a simple model of convection in which particles from the downward flow along the wall are scattered into the central, upward flow at all depths. The flow parameters ξ and τ depend on the frequency and acceleration of the applied vibration; ξ is found to be proportional to the amplitude of a tap, while τ increases exponentially with frequency and appears to diverge as Γ approaches one.

We employed the MRI technique of spin tagging to obtain noninvasive flow profiles of the flow throughout the container. In addition to confirming the tracer particle results for the depth dependence at $r=0$, this method allowed us to determine the radial dependence of the flow. The velocity curvature is fit equally well with either a hyperbolic cosine term or a modified Bessel function of order zero. In both cases, the radial and depth dependences can be combined to find $v(r,z)$ [Eq. (11)].

The MRI data also indicate that the width of the downward flowing region, which determines the threshold size for convectively driven size separation, is independent of both depth and acceleration. It is, however, proportional to container size, so that containers may be sized to control mixing.

At threshold, the convective flow, moving at a velocity scale set by ξ/τ, succombs to a rapidly increasing time scale. This is suggestive of the glass transition, in which a rapid increase in viscosity is unaccompanied by any discernible change in a length scale. More generally, we raise the question of the nature of the onset of convection. Is a dynamic instability of an inherently liquid state occurring, analogous to Rayleigh-Benárd convection, or is a change from a solid to a fluidized state necessary before convection can be initiated?

ACKNOWLEDGMENTS

We wish to thank D. Dawson, S. Esipov, G. Karczmar, C.-h. Liu, N. Menon, J. Miller, and T. Pöschel for enlightening discussions and suggestions. This work is supported in part by the MRSEC program of the National Science Foundation (NSF) under Contract No. DMR-9400379. J.B.K. acknowledges the financial support of the NSF. E.E.E. received financial support from the Grainger Foundation. J.K.F. acknowledges the financial support of the NSF REU program. H.M.J. acknowledges financial support from the David and Lucile Packard Foundation and the Research Corporation.

[1] H. M. Jaeger and S. R. Nagel, Science **255**, 1523 (1992); R. P. Behringer, Nonlinear Sci. Today **3**, 1 (1993); H. Hayakawa, H. Nishimori, S. Sasa, and Y.-h. Taguchi, Jpn. J. Appl. Phys. **34**, 397 (1995).

[2] J. B. Knight, H. M. Jaeger, and S. R. Nagel, Phys. Rev. Lett. **70**, 3728 (1993).

[3] M. Faraday, Philos. Trans. R. Soc. London **52**, 299 (1831).

[4] R. L. Brown, J. Inst. Fuel **13**, 15 (1939); B. J. Ennis, J. Green, and R. Davies, Chem. Eng. Prog. **90**, 32 (1994); T. M. Knowlton, J. W. Carson, G. E. Klinzing, and W.-C. Yang, *ibid.* **90**, 44 (1994); T. Takahashi, Annu. Rev. Fluid Mech. **13**, 57 (1981).

[5] P. K. Haff, J. Fluid Mech. **134**, 401 (1983); J. Rheol. **30**, 931 (1986); in *Granular Matter*, edited by A. Mehta (Springer-Verlag, New York, 1993), pp. 141–160.

[6] S. B. Savage, J. Fluid Mech. **194**, 457 (1988); M. Bourzutschky and J. Miller, Phys. Rev. Lett. **74**, 2216 (1995); H. Hayakawa, S. Yue, and D. C. Hong, *ibid.* **75**, 2328 (1995).

[7] Y-h. Taguchi, Phys. Rev. Lett. **69**, 1367 (1992); J. A. C. Gallas, H. J. Herrmann, and S. Sokolowski, *ibid.* **69**, 1371 (1992); J. Lee, J. Phys. A **27**, L257 (1994).

[8] H. J. Herrman, Physica A **191**, 263 (1992); G. C. Barker and Anita Mehta, Phys. Rev. E **47**, 184 (1993); P. A. Thompson, in *Computer Simulation Studies in Condensed Matter Physics VI*, edited by D. P. Landau, K. K. Mon, and H.-B. Schüttler (Springer-Verlag, Berlin, 1993), pp. 31–45; S. Luding, E. Clement, A. Blumen, J. Rajchenbach, and J. Duran, Phys. Rev. E **50**, R1762 (1994).

[9] T. Pöschel and H. J. Herrman, Europhys. Lett. **29**, 123 (1995).

[10] H. Takahashi, A. Suzuki, and T. Tanaka, Powder Technol. **2**, 65 (1968/69).

[11] P. Evesque and J. Rajchenbach, Phys. Rev. Lett. **62**, 44 (1989).

[12] C. Laroche, S. Douady, and S. Fauve, J. Phys. (France) **50**, 699 (1989); P. Evesque, J. Phys. (Paris) **51**, 697 (1990).

[13] H. K. Pak, E. Van Doorn, and R. P. Behringer, Phys. Rev. Lett. **74**, 4643 (1995).

[14] C. R. Wassgren, C. E. Brennen, and M. L. Hunt, J. Appl. Mech. (to be published).
[15] E. Clement, J. Duran, and J. Rajchenbach, Phys. Rev. Lett. **69**, 1189 (1992).
[16] J. Duran, T. Mazozi, E. Clement, and J. Rajchenbach, Phys. Rev. E **50**, 3092 (1994); **50**, 5138 (1994).
[17] H. M. Jaeger, J. B. Knight, C.-H. Liu, and S. R. Nagel, Mater. Res. Bull. **19**, 25 (1994).
[18] G. Ratkai, Powder Technol. **15**, 187 (1976); C. F. Harwood, *ibid.* **16**, 51 (1977); G. W. Baxter, R. P. Behringer, T. Fagert, and G. A. Johnson, Phys. Rev. Lett. **62**, 2825 (1989).
[19] M. Nakagawa, S. A. Altobelli, A. Caprihan, E. Fukushima, and E.-K. Jeong, Exp. Fluids **16**, 54 (1993).
[20] E. E. Ehrichs, H. M. Jaeger, G. S. Karczmar, J. B. Knight, V. Yu. Kuperman, and S. R. Nagel, Science **267**, 1632 (1995).
[21] The experimental procedure is similar to that in Ref. [2].
[22] Alternatively, we could have reported the RMS value of the tap or the peak acceleration of any one of the other peaks. We have verified that these values all depend linearly on Γ, so that any functional dependence on Γ is independent of our choice to use the peak acceleration.
[23] We have observed that changes in the humidity influence the speed of the convection if the system is not under vacuum. Higher humidity leads to dramatically slower flow.
[24] The experimental procedure is similar to that reported in Ref. [20].
[25] L. Axel and L. Dougherty, Radiology **171**, 841 (1989).
[26] V. Yu. Kuperman, E. E. Ehrichs, H. M. Jaeger, and G. S. Karczmar, Rev. Sci. Instrum. **66**, 4350 (1995).
[27] We are currently working to experimentally characterize the dependence of this roll reversal on wall angle, friction, and acceleration.
[28] That the dependence on r_c drops out can be easily seen in the limit that $R/r_c \gg 1$. In this case $f(R/r_c) \approx \exp(R/r_c)$.
[29] O. Zik and J. Stavans, Europhys. Lett. **16**, 255 (1991).
[30] H. Takahashi and H. Yanai, Powder Technol. **7**, 205 (1973).
[31] R. M. Nedderman and C. Laohakul, Powder Technol. **25**, 91 (1980).
[32] O. Pouliquen and R. Gutfraind, Phys. Rev. E **53**, 552 (1996).
[33] S. B. Savage, J. Fluid Mech. **92**, 53 (1979); J. T. Jenkins and S. B. Savage, *ibid.* **130**, 187 (1983).
[34] J. C. Williams, Fuel Soc. J. **14**, 29 (1963); K. Ahmad and I. J. Smalley, Powder Technol. **8**, 69 (1973); J. Bridgewater, *ibid.* **15**, 215 (1976); J. C. Williams, *ibid.* **15**, 245 (1976); L. T. Fan, Y.-M. Chen, and F. S. Lai, *ibid.* **61**, 255 (1990) and references cited therein.
[35] For other proposed mechanisms of size segregation, see J. B. Knight, H. M. Jaeger, and S. R. Nagel, Ref. [2] and references cited therein; also, G. C. Barker, M. J. Grimson, and A. Mehta in *Powders and Grains '93,* edited by C. Thornton (A. A. Balkema, Rotterdam, 1993), pp. 253–257.